

ANNUAL REPORT

Phase II: Design and Analysis of a Process for Melt Casting Metallic Fuel Pins Incorporating Volatile Actinides

Submitted to

Transmutation Research Program
Technical Focus Area
Fuel Development Research
ATTN: Dr. Anthony Hechanova
Harry Reid Center for Environmental Studies
University of Nevada, Las Vegas

Submitted by

Dr. Yitung Chen, Principal Investigator, uuchen@nye.nscee.edu
Dr. Randy Clarksean, Co-Principal Investigator, rclark@lakesplus.com
Dr. Darrell W. Pepper, Co-Principal Investigator, pepperu@nye.nscee.edu
Department of Mechanical Engineering
University of Nevada, Las Vegas
4505 Maryland Parkway, Box 454027
Las Vegas, NV 89154-4027
Phone: (702) 895-1202
Fax: (702) 895-3936

Collaborators

Dr. Mitchell K. Meyer, Leader of Fabrication Development Group
Dr. Steven L. Hayes, Manager of Fuels & Reactor Materials Section
Nuclear Technology Division
Argonne National Laboratory, Idaho Falls, ID

Phase II Project Dates: 5/1/02 – 4/30/03

June 15, 2003

Table of Contents

1. Introduction	5
2. Project Overview	6
3. Furnace Models	7
3.1 Casting Rod Heat Transfer Model.....	8
3.1.1. Physical And Numerical Model	8
3.1.2. Governing Equations	10
3.1.3. FIDAP Details	11
3.1.4. Volume of Fluid (VOF) Method	13
3.1.5. Results.....	14
3.2 Induction Heating Model.....	24
3.2.1. Modeling Results	24
3.2.2. Theoretical Background	29
3.3 Mass Transfer Model.....	30
4. Summary	32
5. References.....	33
6. Appendices.....	38

List of Figures

Figure 1 - Schematic of proposed induction skull melting furnace for the casting of high americium content fuels.....	7
Figure 2 - The Schematic of fuel rod casting model.....	9
Figure 3 - Axisymmetric geometry of the fuel rod casting model.....	9
Figure 4 - Calculation of total energy stored by a <i>quartz glass</i> mold compared to the amount of energy contained within the melt for different initial mold temperatures. Above the solid line indicates the mold has adequate thermal storage to solidify all of the melt. (Melt is at 1500°C, $r_{pin} = 0.004$ m).....	15
Figure 5 - Calculation of total energy stored by a <i>copper</i> mold compared to the amount of energy contained within the melt for different initial mold temperatures. (Melt is at 1500°C, $r_{pin} = 0.004$ m).....	16
Figure 6 - Temperature profiles for flow through the mold prior to solidification for a constant pressure inlet boundary condition. Dashed line represents the temperature at which phase change occurs. (Inlet pressure = 20,000 Pascal, Mold temperature = 400°C, initial melt temperature = 1500°C, interfacial heat transfer coefficient = 2,000 W/m ² K).....	17
Figure 7 - Temperature profiles for the heating of the mold during the cooling and solidification of the melt. (Inlet pressure = 20,000 Pascal, Mold temperature = 400°C, initial melt temperature = 1500°C, interfacial heat transfer coefficient = 2,000 W/m ² K).....	18
Figure 8 - Axial velocity profile for constant inlet pressure of 20,000 Pa (Mold temperature = 400°C, initial melt temperature = 1500°C, interfacial heat transfer coefficient = 2,000 W/m ² K)..	18
Figure 9 - Axial velocity profile for constant inlet pressure of 20,000 Pa and a higher heat transfer coefficient than Figure 7 (Mold temperature = 400°C, initial melt temperature = 1500°C, interfacial heat transfer coefficient = 5,000 W/m ² K).....	19
Figure 10 - Axial velocity profile for constant inlet pressure of 400,000 Pa (Mold temperature = 800°C, initial melt temperature = 1500°C, interfacial heat transfer coefficient = 2,000 W/m ² K)..	20
Figure 11 - Representative results for flow solidification study to aid in understanding numerical aspects of flow solidification in mold (Mold temperature = 400°C, initial melt temperature = 1500°C, interfacial heat transfer coefficient = 2,000 W/m ² K).....	20
Figure 12 - Comparison of solidification front for different heat transfer coefficients (Inlet pressure: P= 20,000 Pa; inlet temperature= 1500°C; mold preheated temperature: T=400°C; phase change temperature: 1400-1410°C; mold material: copper).....	21
Figure 13 - Comparison of solidification front advancement for different mold materials (Inlet pressure: P= 20,000 Pa; inlet temperature= 1500°C; mold preheated temperature: T=400°C; convection heat transfer coefficient h = 2,000 W/m ² °C; phase change temperature: 1400-1410°C).....	22
Figure 14 - Comparison of average filling velocity for different heat transfer coefficients (Inlet pressure: P= 20,000 Pa; inlet temperature= 1500°C; mold preheated temperature: T=400°C; phase change temperature: 1400-1410°C; mold material: copper).....	22
Figure 15 - Comparison of average velocity of the melt as it flows into the mold for different mold materials. (Inlet pressure: P= 20,000 Pa; inlet temperature= 1500°C; mold preheated temperature: T=400°C; phase change temperature: 1400-1410°C).....	23

Figure 16 - Representative flow field for free surface flow into mold region (axisymmetric geometry shown). Solid line across the velocity vectors represents the fill front. (0.01 seconds between plots, Inlet velocity $V=0.5$ m/s, Mold material: copper, Inlet temperature: $1,500^{\circ}\text{C}$ Heat transfer coefficient $h=2,000$ $\text{W}/\text{m}^2\text{C}$ Mold preheated temperature 800°C).....24

Figure 17 - Representative system model for ISM.....25

Figure 18 - Finite element mesh for the analysis of induction heating in an ISM system.....26

Figure 19 - Contour plots of the field variable C used in the calculation of the induction heating equation.....27

Figure 20 - Surface plot of the field variable C used in the calculation of the induction heating equation. Each peak resides at the location of a coil of the induction coil.....27

Figure 21 - Contours of field variable S (species 2) used in the calculation of the induction field. Peak occurs near the top edge of the melt region.....28

Figure 22 - Surface plot of induction heating field variable S. Peak occurs at the outer edge and top of the melt region.....28

Figure 23 - Mass transport consists of (1) transport within the melt, (2) vaporization at the interface, and (3) transport in the gas phase.....31

1. Introduction

The United States is embarking on a national program to develop transmutation of high-level radioactive waste as part of the Advanced Fuel Cycle Initiative (AFCI) at its national laboratories. Through the AFCI Program, the U.S. joins international efforts to evaluate the potential of partitioning and transmutation along with advanced nuclear fuel cycles. Transmutation means nuclear transformation that changes the contents of the nucleus (protons and/or neutrons). The research and development efforts will consider a coupled accelerator and sub-critical multiplying assembly, explore the transmutation of waste from used nuclear fuel, testing of advanced nuclear fuels, and the production of isotopes that may be required for national security and commercial applications.

The AFCI program requires a non-fertile actinide form to serve as the “fuel” for the transmuter blanket. The AFCI program has listed several critical issues in fuel requirements: cladding integrity, fission product retention, and dimensional, chemical, and metallurgical stability during irradiation under both normal and off-normal conditions. The currently proposed candidates for this fuel form still include a metallic alloy fuel, a cermet fuel, and a nitride fuel. Each of these candidates has been proposed based on known performance of the fertile fuel (i.e., uranium) analogue. One of the potential fuel types is a metallic fuel, which is being developed by Argonne National Laboratory. An important aspect of this program is the development of a casting process by which volatile actinide elements (i.e., americium) can be easily incorporated into metallic fuel pins. The process relies on a traditional casting process using induction heating and quartz glass, copper or stainless steel rods as molds. This process works well for the fabrication of metal fuel pins traditionally composed of alloys of uranium and plutonium, but does not work well when highly volatile actinides (i.e., americium) are included in the melt. Previous experience with this process indicates that there is the potential for large losses of americium.

The present process relies on a pressure/gravity-driving casting procedure that is briefly overviewed here. The process relies on the use of quartz glass, copper or stainless steel molds which are long, thin and straw-like tubes. The crucible cover was added to aid in controlling the transport of americium from the melt. The feed-stock, which consists of the end pieces chopped from previously cast fuel slugs, leftover fragments from previous casting, rejected slugs, and fresh feedstock (including actinides, americium, plutonium and zirconium), is loaded into the crucible. The feed-stock is inductively heated until it is melted. Then the molten melt flows into the mold by gravity or through rapid pressurization if a controlled filling pressure is expected. The resistance heaters were employed to preheat of the molds to a desired temperature in order to ensure the melt flows into the whole molds before it solidifies. The casting process takes less than a second. Once filled, the molds are withdrawn from the pallet and cooled - producing about a hundred metallic fuel pins - all in one operation.

The americium loss most likely occurs both during the extended time period required to superheat the alloy melt as well as when the chamber must be evacuated. The high vapor-pressure actinides, particularly americium, are susceptible to rapidly vaporize and transport

throughout the casting furnaces, resulting in only a fraction of the charge being incorporated into the fuel pins as desired. This is undesirable both from a materials accountability standpoint as well as from the failure to achieve the objectives of including these actinides in the fuel for transmutation. Americium volatility during fabrication and irradiation, and actinide compatibility with cladding are also very important fuel issues. The chamber pressure could be increased to decrease the evaporation of americium. Inert gas (usually Ar) can be filled in the chamber, since the addition of an inert gas in a chamber increases the recondensation of the volatile elements and consequently reduces the americium evaporation losses. Another technique might be to react the americium to another material to form a material that has a higher vapor pressure.

This research report develops a model to analyze the transport of americium from the melt to the vapor phase above the crucible. The model considers mass transport in the melt, vaporization at the surface, and transport through the vapor phase. The greatest problem with the model is the uncertainty of the thermodynamic properties of the proposed ternary alloy. The details of the model and the specific quantities needed for the physical properties will be discussed.

2. Project Overview

Figure 1 shows a schematic of the proposed furnace design to cast metallic fuel pins that contain americium. The system consists of an induction skull melter, a crucible cover, “chill” molds, and resistance heaters to control the preheating of the molds. The crucible cover was selected to aid in controlling the transport of americium from the melt. Chill molds were selected over continuous casting to insure proper geometric control, and the resistance heaters were added to insure that preheating of the molds could be controlled to insure the melt will flow into the mold.

Several basic phenomena exist in the proposed furnace and need to be analyzed. These phenomenon include

- Transport of americium from the melt into the upper regions of the crucible region,
- Impact of induction heating on the flow and heating of the melt material, and
- The flow of melt into the chill molds.

The present paper addresses this last phenomenon, the flow and heat transfer associated with the melt entering the chill molds. The important physics of this process includes

- Heat transfer from the melt into the mold,
- Mold size, shape and material,
- Preheating of the molds,
- Mechanism to force the flow into the molds (pressure injection vs. gravity), and
- Phase change characteristics of the melt.

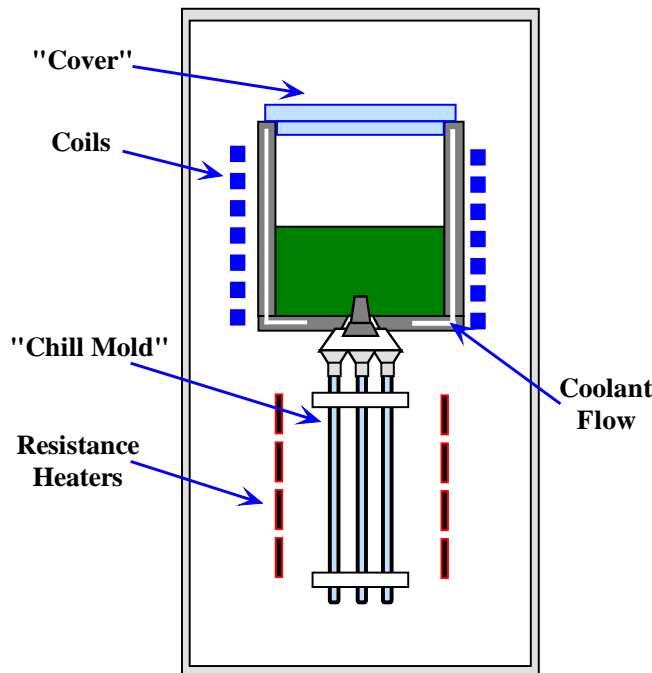


Figure 1 - Schematic of proposed induction skull melting furnace for the casting of high americium content fuels.

The primary difference between the ISM and other casting furnaces is the nature of the crucible. The crucible is a slotted, cooled copper design. Great melting efficiencies could be achieved by splitting the crucible into a multi-segments crucible. Also the increased number of crucible segments renders the crucible discontinuous enough to levitate the melt sufficiently to prevent excessive arcing and resulting crucible damage. The oxygen and nitrogen contamination during the melting process is also eliminated due to the skull crucible. The crucible cover was selected to aid in controlling the transport of americium from the melt. The resistance heaters were added to insure that preheating of the molds could be controlled to insure the melt will flow into the molds. In ISM, the induction fields and constant intense stirring of metal maintain a high level of superheat throughout the melt, so the temperature of the initial metal poured is virtually identical to the temperature of the final metal poured from a heat and a high purity melt can be achieved. Chill molds were selected over continuous casting to insure proper geometric control. The melt will flow into the molds either by gravity or through pressurization. These two cases are simulated to see which one is better. The copper molds and quartz molds options are also analyzed to determine a better selection.

3. Furnace Models

Three general purpose models are needed to effectively analyze the proposed induction skull melter design. These include

- The analysis of the flow and solidification into a “chill” mold,

- The evaluation of the induction heating within the furnace, and
- Assessment of the mass transfer within the crucible system.

Each of these models will be addressed below. Numerical results of the casting process are presented and briefly discussed. The induction-heating model is also presented along with preliminary modeling results for a realistic geometry (coils, melt, crucible). A detailed mass transfer model is then outlined and discussed.

3.1 Casting Rod Heat Transfer Model

The casting rod model considers the flow of the melt into a chill mold. The fluid is assumed to enter the mold at a constant velocity. As the flow enters the mold it is cooled and will begin solidification. The model has been setup to allow for the parametric variation of important physical parameters.

3.1.1. Physical And Numerical Model

Much of the details of the numerical model have not significantly changed from last year, but more modeling has been completed to understand the physical processes behind the flow and solidification of molten metal into the mold.

First, the details of the physical model and the simplifying assumptions will be presented. Second, the governing equations for the numerical model will be presented. These equations are solved using a commercially available finite element method FIDAP (product of Fluent, Inc.). That will be followed by a discussion of the VOF (Volume of Fluid) method.

A schematic diagram (Figure 1) shows the general geometry of the induction skull melter (ISM) furnace, which consists of an induction skull melter, a crucible cover, “chill” molds and resistance heaters. The crucible cover will be helpful to control the transport of americium from the melt. Chill molds were selected over continuous casting to insure proper geometric control. We use resistance heaters to control the molds preheating temperature, which makes sure the melt will flow into the molds.

This section of the report addresses the flow and heat transfer associated with the melt entering the chill molds. The important physics of this process includes

- Heat transfer from the melt into the mold,
- Mold size, shape and material,
- Preheating of the molds,
- Mechanism to force the flow into the molds (pressure injection vs. gravity), and
- Phase change characteristics of the melt.

As the crucible heats up, the plutonium, americium, and zirconium feedstock melts. The melt is then magnetically stirred to assure homogeneity of the melt before casting. When the proper temperature is reached, the melt will flow into the molds. A number of different velocities will

be assumed to study how rapidly the melt must flow into the molds in order to prevent solidification prior to reaching the end of the mold. It is assumed that the melt flows out of the crucible and down into the molds.

Figure 2 shows the geometry of the mold model with one end closed. The total length of the mold varies in the simulations, but ranges from 0.5 to 1.0 meter to find out what range of length we can produce with low americium loss. The inner radius of the mold is 4 millimeters and the outer radius is 8 millimeters. The molds are preheated before the molten fluid fills the molds. The molds are preheated to insure that the melt flows nearly the full length of the mold, giving the desired rod length.

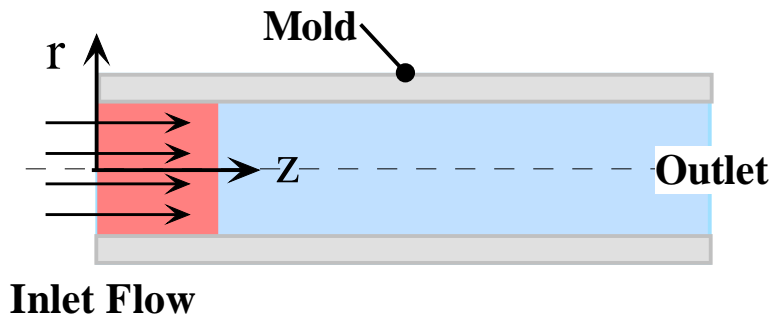


Figure 2 - The Schematic of fuel rod casting model

The molds have a cylindrical shape, which can be reduced to axisymmetric geometry involving radial and axial components. Figure 3 shows the simplified geometry. Whenever possible, the use of an axisymmetric geometry reduces the computational times. The variables that will affect mold filling are the average fill velocity of melt, initial mold temperatures and the heat transfer coefficient between the melt and the mold. The filling process happens only within a few seconds. The heat transfer coefficient between the melt and the mold is an important factor affecting the heat transfer.

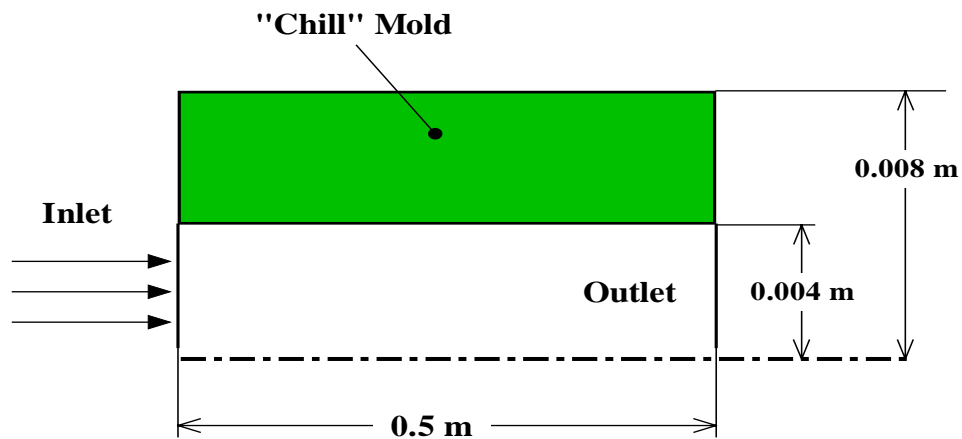


Figure 3 - Axisymmetric geometry of the fuel rod casting model.

3.1.2. Governing Equations

The governing equations for the transient analyses of the melting of the phase change material included the Navier-Stokes (momentum) equations, the continuity equation, and the energy equation. Figure 3 shows a schematic of the model, which includes the melt and the mold. The important physics of the problem include the heat transfer into the mold, cooling of the melt, thermal mass of the mold, and the necessary forces to cause the melt to flow into the mold. An axisymmetric model can capture all of these phenomena.

The problem will be analyzed numerically through the use of the commercial finite element package FIDAP™. This package is a general-purpose heat transfer and fluid mechanics code.

These equations are shown in tensor notation below.

$$\rho \frac{\partial \vec{u}}{\partial t} + \rho(\vec{u} \cdot \nabla)\vec{u} = -\nabla p + \mu \nabla^2 \vec{u} \quad (1)$$

$$\nabla \cdot \vec{u} = 0 \quad (2)$$

$$\rho C_p \frac{\partial T}{\partial t} + \rho C_p \vec{u} \cdot \nabla T = k \nabla^2 T \quad (3)$$

At the interface between the solid and the liquid the conditions of equal temperatures between the interfaces and the heat transfer between the phases include the latent heat release. These two relationships are shown below in equation form.

$$T_l = T_s \quad (4)$$

$$k_l \frac{\partial T_l}{\partial n^*} - k_s \frac{\partial T_s}{\partial n^*} = \rho_s L u^* \quad (5)$$

The condition of a no-slip velocity for the liquid phase is also imposed at the interface between the melt and the solidified melt. This means all the velocity components are zero in the interface.

Phase change was modeled through the use of the “slope” method within FIDAP. In general, the slope method uses the slope of the enthalpy-temperature curve to define a specific heat of the material of interest. The enthalpy of a material that changes phase at a temperature T_m is defined as

$$H(T) = \int_{T_{ref}}^T (C_p(T) + L\eta(T - T_m)) dT \quad (6)$$

where

$$\eta(T - T_m) = \begin{cases} 1 & \text{if } (T - T_m) \geq 0 \\ 0 & \text{if } (T - T_m) < 0 \end{cases} \quad (7)$$

An equivalent specific heat can be defined as the derivative of the enthalpy function, given as

$$C_{equiv} = \frac{dH}{dT} = C_p(T) + L\delta(T - T_m) \quad (8)$$

For pure liquids, phase change occurs at a constant temperature. To approximate this process numerically, the slope method requires the definition of a finite temperature difference over which the phase change occurs. Without defining a small temperature difference, the specific heat determined from the enthalpy-temperature curve is infinite. To numerically implement the relationship shown above for the finite element technique, the following modification is made

$$C_{equiv} = C_p(T) + L\delta^*(T - T_m, \Delta T) \quad (9)$$

where $\delta^*(T - T_m, \Delta T)$ has a large but finite value over the temperature range $(T_m - \Delta T/2)$ to $(T_m + \Delta T/2)$ and is zero outside this range. The use of this “artificial” specific heat allows for the correct amount of energy removal to occur from an element before it is considered to be a solid. Physically, the total energy transfer required for phase change is correct.

Conduction within the solid (mold) required the solution of the conduction equation, which is shown below.

$$\rho C_p \frac{\partial T}{\partial t} = k \nabla^2 T \quad (10)$$

At the interface between the solid and the adjacent molten material, the conditions of equal temperature and energy conservation are required. The interface temperature does not have to match identically because a convective heat transfer relationship is used to model the interface between the melt and the mold. This technique is commonly used in casting analysis.

$$k_{m_t} \frac{\partial T_{m_t}}{\partial n} = k_l \frac{\partial T_l}{\partial n} \quad (11)$$

3.1.3. FIDAP Details

The finite element method is a well-known numerical method. The interesting aspect of the finite element method is that the problem formulation results in a system of simultaneous algebraic equations instead of a system of differential equations. This is because a system or a body is

modeled by subdividing into smaller elements. Finite element analysis involves the following steps, [15]:

- Specify the geometry and divide domain into finite elements (small local regions where the governing equations are approximated)
- Formulate the properties of each element and determine the node properties using known information
- Assemble elements to obtain the finite element model of the domain
- Apply the known values – boundary and initial condition.
- Specify how the domain is affected by the known nodes
- Solve simultaneous linear algebraic equations to determine node transport properties (temperature, velocity, pressure, etc.)

The power of the finite element method resides principally in its versatility. The method can be applied to various physical problems. The body analyzed can have arbitrary initial and boundary conditions. The mesh can mix elements of different types, shapes, and physical properties. This great versatility is contained within a single computer program. User-prepared input data controls the selection of problem type, geometry, boundary conditions, and element selection. Another attractive feature of finite elements is the close physical resemblance between the actual system and its finite element model.

The finite element method also has disadvantages. A computer, a reliable program, and intelligent use are essential. A general-purpose program has extensive documentation, which cannot be ignored. Experience and good engineering judgment are needed in order to define a good model. Many input data are required and voluminous output must be stored and understood. [15]

An iterative solution technique for a FEM solver was employed to solve the set of equations sequentially and separately for each active degree of freedom. This approach is referred to as a segregated solver. This method is used because it substantially reduces the memory requirement compared to the other solvers used, such as the fully coupled method. FIDAP uses the VOF (Volume of Fluid) technique to model transient flows involving free surfaces of arbitrary shape. The capabilities constitute a powerful tool in simulating complex free surface deformations including folding and breakup.

FIDAP was used to solve the fluid and heat flow inside the molds. A “mapped” type mesh was used to discretize the geometry. The general purpose pre-processor GAMBIT™ was used for the mesh generation.

A mapped mesh is a regular “checkerboard” mesh for surface areas that are typically used for more regular geometries. The complete finite element mesh for the heat transfer problem was constructed from a collection of mapped mesh areas. This technique is not automatic, as the geometry must be decomposed into regions that are suited to a mapped mesh.

A backward Euler (implicit) scheme was used to solve the three transient equations. Segregated iterative method was used to obtain the solution at each time step using fixed time step.

Although one can generally obtain high order accuracy, when convection is strong compared to the diffusion and sharp gradients of the flow variables are encountered in the computational grid, unstable results are likely to occur. Streamline upwinding is used to stabilize the oscillations in the computations.

There are two general approaches that could be used to model the flow of the molten material into the melt. The first is to move the mesh with the melt. This approach requires the mesh to be continually recalculated and it requires a technique to couple the heat transfer to the solid. The second choice is to have the fluid move through a fixed mesh. This latter technique is the approach FIDAP uses and it will briefly be discussed next.

3.1.4. Volume of Fluid (VOF) Method

Free boundaries are considered to be surfaces on which discontinuities exist in one or more variables. Examples are free surfaces of fluids (open channel flow), material interfaces, shock waves, or interface between a fluid and deformable structures. Three types of problems arise in the numerical treatment of free boundaries: (1) their discrete representation, (2) their evolution in time, and (3) the manner in which boundary conditions are imposed on them. The process of embedding a discontinuous surface in a matrix of computational cells involves three separate tasks. First, it is necessary to devise a means of numerically describing the location and shape of the boundary. Second, an algorithm must be given for computing the time evolution of the boundary. Finally, a scheme must be provided for imposing the desired surface boundary conditions on the surrounding computational mesh. [16]

FIDAP uses the Volume of Fluid (VOF) method as a technique to simulate free surface flows. [17] This tool is a filling process, which allows the simulation of complex free surface flows with an arbitrary shape in any situation including folding or break-up. The filling process is computed as follows:

- A Galerkin finite element method is used to resolve Navier-Stokes equations.
- Free surfaces are characterized by a VOF type representation on the mesh, advection of the fluid is followed by a volume tracking method.
- On the basis of a given velocity field, a new fluid boundary is determined with the volume method. When the new fluid boundary is obtained, the Reynolds Average Navier-Stokes equations are solved using a finite element method. These two methods are thus applied in alternating deformations and decoupled in order to predict transient deformations.

The VOF technique relies on the definition of a variable F whose value is unity at any point occupied by fluid and zero otherwise. The average value of F in a cell would then represent the fractional volume of the cell occupied by fluid. In particular, a unit value of F would correspond to a cell full of fluid, while a zero value would indicate that the cell contained no fluid. Cells with F values between zero and one must then contain a free surface. VOF method only requires one storage word for each mesh cell, which is consistent with the storage requirements for all other dependent variables.

The indicator function F represents the fluid volume, which is moved by the flow field. So the advection of the this function is governed by:

$$\frac{\partial F}{\partial t} + \bar{V} \cdot \bar{\nabla} F = 0 \quad (12)$$

The sharp interfaces are maintained by ensuring a sharp gradient of F . The value of this function is 1 when the cell of the meshing volume is filled and is equal to 0 when this cell is emptied. A steep gradient of F represents a free surface location.

$$F(\bar{x}, t) = \begin{cases} 1 & \text{Fluid} \\ 0 & \text{Void} \end{cases} \quad (13)$$

The function F can be discretized as follows:

$$f_i = \frac{1}{V_i} \int F dV_i \quad \text{for element I} \quad (14)$$

The limits of integration are restricted to the volume of an element V_i . The value of f_i corresponds to a filled state, an emptied state, or fractional filled state. Thus f_i varies between 0 and 1. An element whose $f_i = 1$ is referred to as a filled element. An emptied element is denoted by $f_i = 0$. The value of f_i between 0 and 1 means a fractional fill or a free surface. [17][18]

The VOF method offers a region-following scheme with smaller storage requirements. Furthermore, because it follows regions rather than surface, all logic problems associated with intersecting surfaces are avoided with the VOF technique. The method is also applicable to three-dimensional computations, where its conservative use of stored information is highly advantageous. In principle, the method can be used to track surfaces of discontinuity in materials properties, in tangential velocity, or any other property. The particular case being represented determines the specific situations that must be applied at the location of the boundary. For situations where the surface does not remain fixed in the fluid, but has some additional relative motion, the equation of motion must be modified. Examples of such applications are shock waves, chemical reaction fronts, and boundaries between single-phase and two-phase fluid regions. [16]

3.1.5. Results

Three different mold materials were selected for analysis. The thermal properties for these mold materials are shown in Table 1. Copper was chosen because of its good heat transfer properties. Quartz glass is listed because it has been traditionally used for injection casting of fuel pins. Stainless steel is listed because it typically has good high temperature properties. In addition, these three materials have a range of thermal diffusivities – representative of other materials that could potentially be used for the molds.

Table 1 - Thermal properties for mold materials.

	<u>Copper</u>	<u>Stainless Steel</u>	<u>Quartz Glass</u>
Thermal Conductivity(W/m ^o C)	320	24	1.4
Specific Heat (J/Kg ^o C)	380	461	670
Density (Kg/m ³)	8933	7750	2200
Thermal Diffusivity (m ² /sec)	9.4E-05	6.7E-06	9.5E-07

A simple thermal model was developed to analyze the total thermal mass of the mold. The intent of the model was to only show if a mold would be able to solidify all of the melt without the need for additional cooling.

Figure 4 shows a plot of total energy storage capacity for a mold that contains the melt for a fuel pin with a 0.004 m radius. The energy storage capacity of the mold increases as the mold radius increases (x-axis). The solid line on the graph is the amount of energy what would have to be stored in order to completely solidify the melt at an initial temperature of 1500°C.

Figure 5 shows similar results for a copper mold system. Figures 4 and 5 clearly indicate that even for relatively high preheat temperatures the mold will have enough thermal capacity to solidify all of the melt that flows into the mold. *This implies that the solidification of the melt strictly depends on the heat transfer from the melt into the mold.*

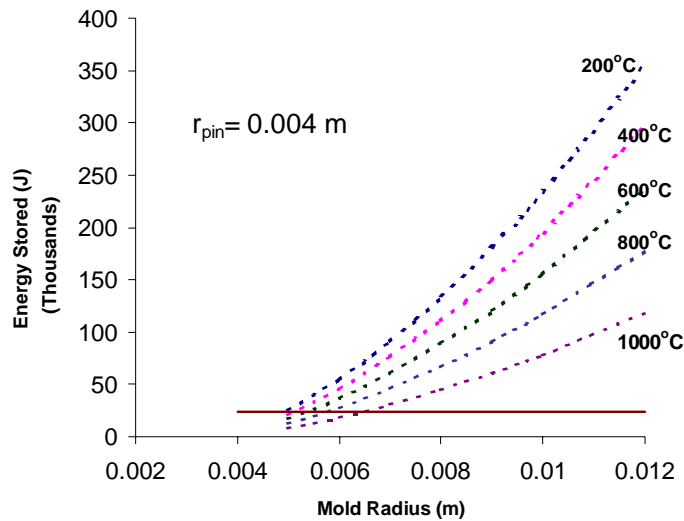


Figure 4 - Calculation of total energy stored by a quartz glass mold compared to the amount of energy contained within the melt for different initial mold temperatures. Above the solid line indicates the mold has adequate thermal storage to solidify all of the melt. (Melt is at 1500°C, $r_{pin} = 0.004$ m)

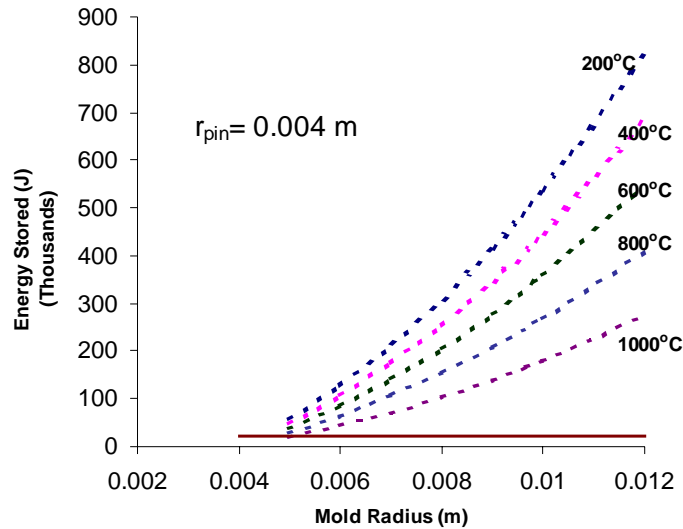


Figure 5 - Calculation of total energy stored by a *copper* mold compared to the amount of energy contained within the melt for different initial mold temperatures. (Melt is at 1500°C, $r_{pin} = 0.004$ m)

The second set of analyses considers the mold to be filled with molten material. The inlet boundary condition can be either constant velocity, or a constant pressure condition. This type of analysis gives insight into the time scales one must consider for the solidification of the melt once it is in the mold. The second set of analyses considered the filling of the mold. The completion of this task will include the filling and solidification of the mold at the same time through the use of the VOF technique.

Figures 6 and 7 show typical cooling and solidification profiles for a representative simulation. The results shown are for a constant pressure inlet condition of 20,000 Pa, mold heat transfer coefficient of 2,000 W/m²K, and an initial mold temperature of 400°C. The dashed line in Figure 6 represents the phase change temperature for the simulation. Conduction only occurs within the solidified material as indicated by the nearly linear profiles. Figure 7 shows the heat up of the mold as a function of time. The heat capacity of the mold is much greater than the heat capacity of the molten material as shown in Figures 4 and 5. The mold material is assumed to have properties similar to that of copper. The intent of the modeling is to assist in the design of the molds from a materials property standpoint and from a structural standpoint. The mold must be able to maintain its shape without warping while the melt solidifies.

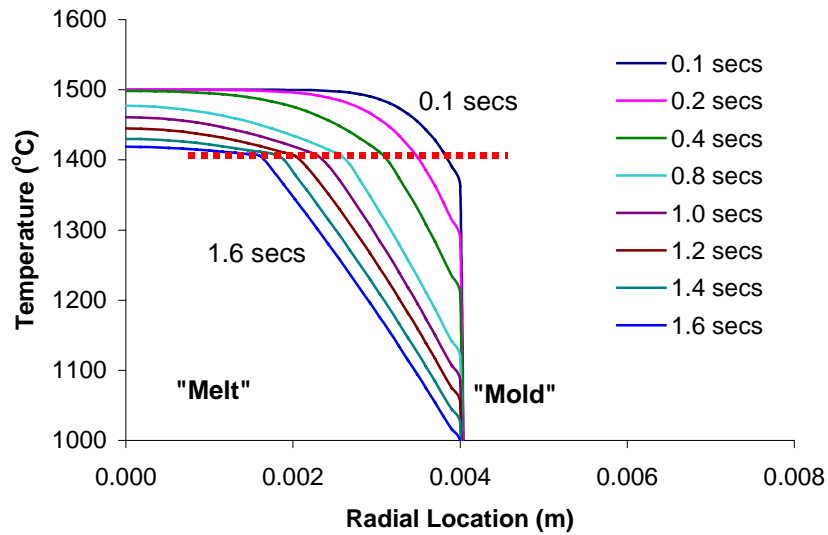


Figure 6 - Temperature profiles for flow through the mold prior to solidification for a constant pressure inlet boundary condition. Dashed line represents the temperature at which phase change occurs. (Inlet pressure = 20,000 Pascal, Mold temperature = 400°C, initial melt temperature = 1500°C, interfacial heat transfer coefficient = 2,000 W/m² K)

Figure 8 shows how the flow increases in velocity and then starts to decrease in velocity as the melt starts to solidify. A constant pressure boundary condition is representative of the injection casting process where pressure is suddenly ramped up, forcing the molten material into a mold.

The flow starts from a plug flow shape, slowly moves to more of a parabolic shape, and then remains nearly parabolic as the total flow decreases as the melt solidifies towards the center of the geometry. All of these results are for a constant pressure inlet condition. Previous work examined constant velocity conditions. The constant pressure condition is more realistic because of the injection casting process.

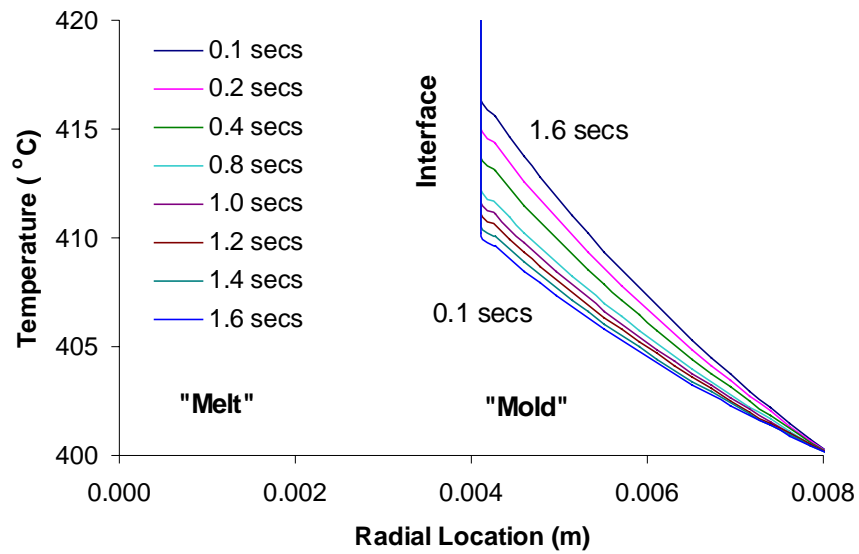


Figure 7 – Temperature profiles for the heating of the mold during the cooling and solidification of the melt. (Inlet pressure = 20,000 Pascal, Mold temperature = 400°C, initial melt temperature = 1500°C, interfacial heat transfer coefficient = 2,000 W/m² K)

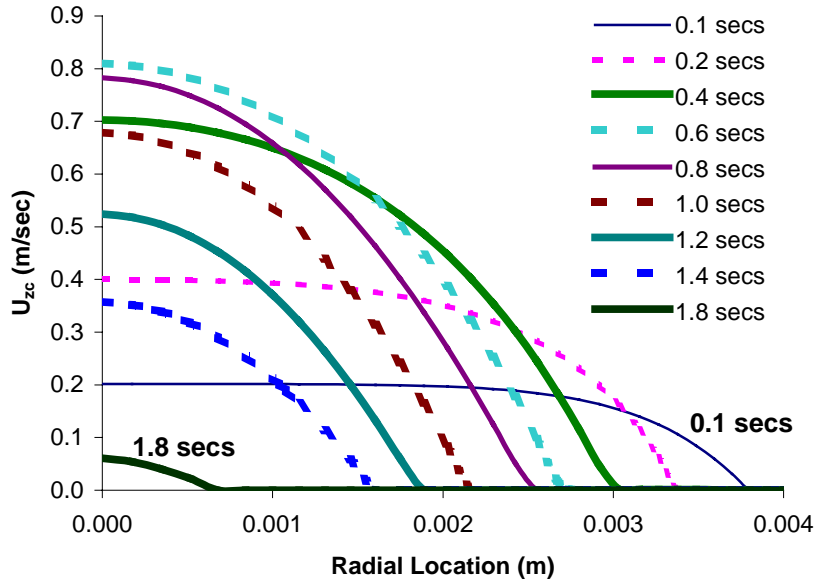


Figure 8 – Axial velocity profile for constant inlet pressure of 20,000 Pa (Mold temperature = 400°C, initial melt temperature = 1500°C, interfacial heat transfer coefficient = 2,000 W/m² K).

Figure 9 presents the flow field for a higher heat transfer coefficient and the same inlet pressure. Increasing the heat transfer decreases the peak velocity experienced during the flow and

solidification of the melt. The actual heat transfer rates between the mold and the melt are not known for the present concept because no experimental tests exist on the particular melt mold interface. Therefore, the impact of this parameter is studied and analyzed.

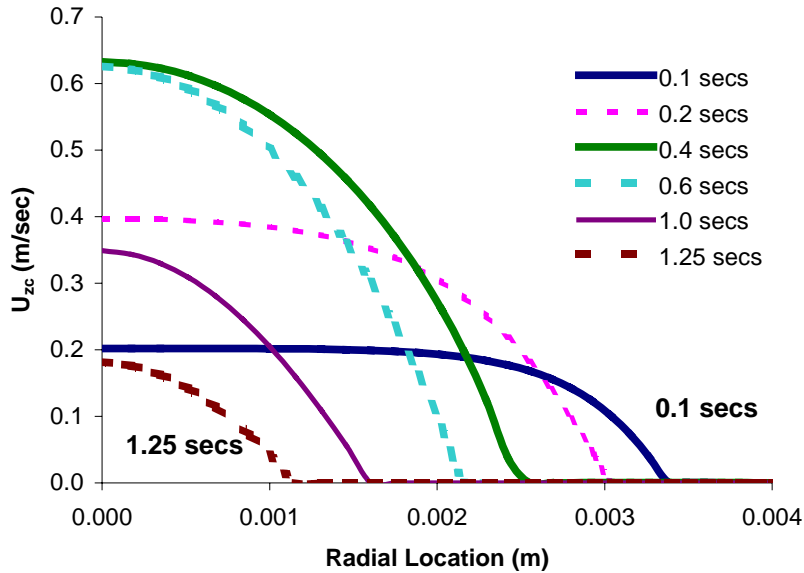


Figure 9 - Axial velocity profile for constant inlet pressure of 20,000 Pa and a higher heat transfer coefficient than Figure 7 (Mold temperature = 400°C, initial melt temperature = 1500°C, interfacial heat transfer coefficient = 5,000 W/m² K).

The impact of injection pressure can also be studied as shown in Figure 10. The results here are for an injection pressure at nearly 4 atmospheres. The mold temperature is also lower. The peak velocity is 1-2 orders of magnitude larger.

Figure 11 shows the advancement of the solidification front for an inlet pressure of 20,000 Pa, heat transfer coefficient of 2,000 W/m²K, and a mold temperature of 400°C. The front moves slowly into the melt.

The impact of the heat transfer on melt solidification can be found in Figure 12. This figure reports the location of the solidification front as the flow solidifies. The distance is the radial distance from the centerline of the solidification front. Some of the material quickly solidifies by the wall, and then continues to solidify slowly until the radius becomes small. Once the diameter becomes roughly 25 percent of the outer diameter, the flow quickly solidifies and stops. Slow cooling occurs after this time.

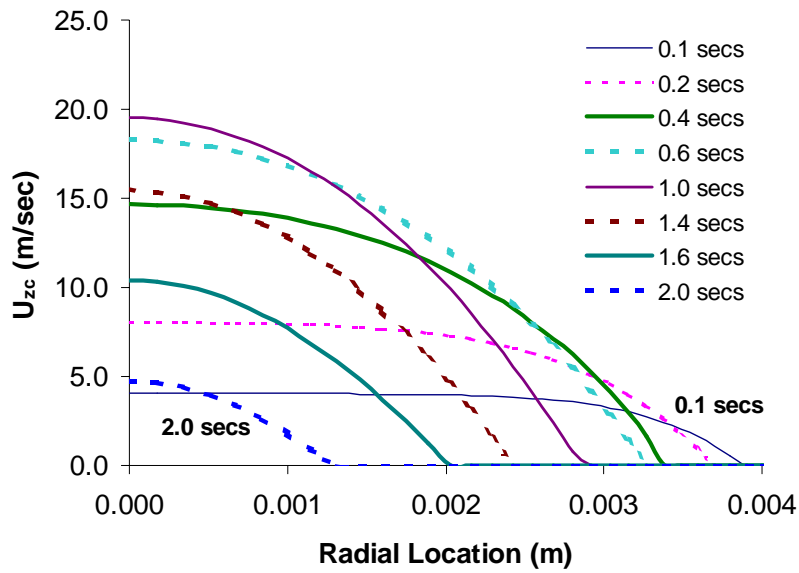


Figure 10 - Axial velocity profile for constant inlet pressure of 400,000 Pa (Mold temperature = 800°C, initial melt temperature = 1500°C, interfacial heat transfer coefficient = 2,000 W/m² K).

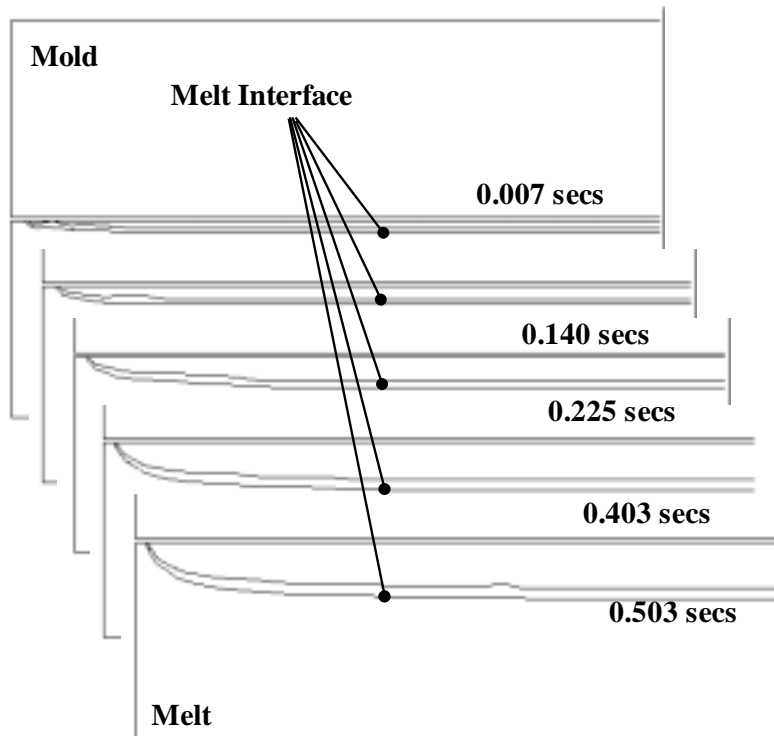


Figure 11 - Representative results for flow solidification study to aid in understanding numerical aspects of flow solidification in mold (Mold temperature = 400°C, initial melt temperature = 1500°C, interfacial heat transfer coefficient = 2,000 W/m² K).

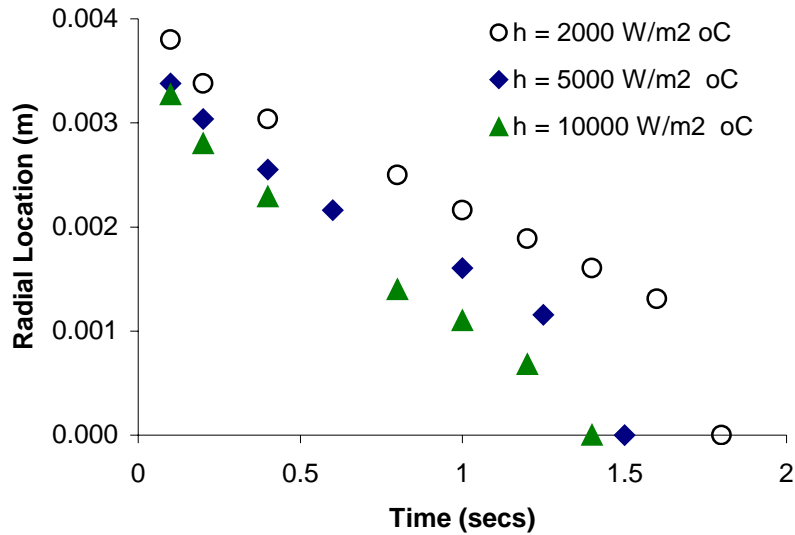


Figure 12 – Comparison of solidification front for different heat transfer coefficients (Inlet pressure: $P= 20,000$ Pa; inlet temperature= 1500°C ; mold preheated temperature: $T=400^{\circ}\text{C}$; phase change temperature: $1400\text{-}1410^{\circ}\text{C}$; mold material: copper).

Figure 13 shows the impact of mold material on the advancement of the solidification front. As expected, the mold material can have a significant impact on the solidification time for a melt flowing through a mold. A factor of two change in solidification times is noted for typical materials.

Figure 14 goes a step farther and examines the impact the interfacial heat transfer coefficient has on the flow rate of material into the mold for a constant pressure inlet condition. A factor of 5 change in the heat transfer coefficient does not lead to a similar change in average velocities. The velocity of the flow into the mold will be greatly impacted by the movement of the solidification front. As the front advances, the resistance to the flow increases, and ultimately slows the flow and leads to the stoppage of the flow. Figure 15 shows the impact of mold material on the average fill velocity as well.

It is interesting to note that the maximum velocity depends mostly on the pressure, and not the mold material. The material accelerates, fills the mold, and then the velocity starts to slow. The rate at which the flow slows down and hence solidifies is clearly determined by the material type.

Figures 12 to 15 imply that a factor in the solidification rate is the rate at which heat can be transferred into the mold. This limitation may ultimately determine the mold design and casting process parameters.

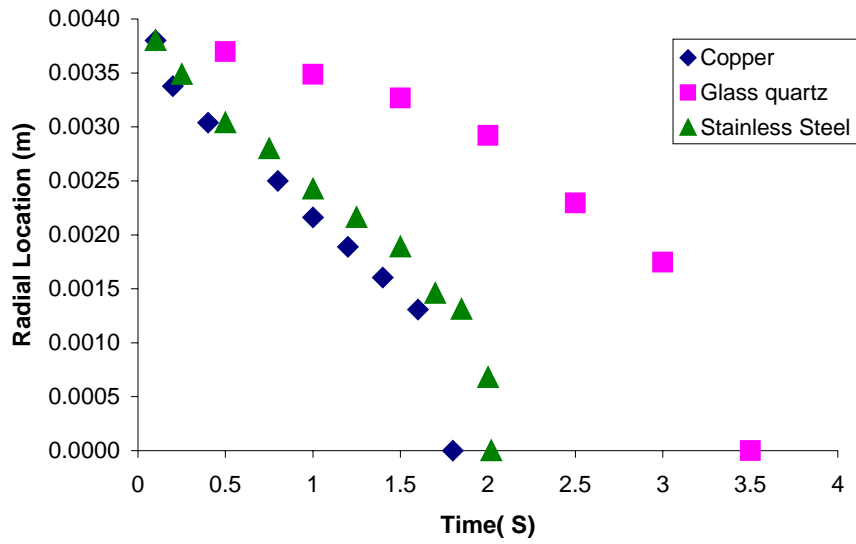


Figure 13 - Comparison of solidification front advancement for different mold materials (Inlet pressure: $P= 20,000$ Pa; inlet temperature= 1500°C ; mold preheated temperature: $T=400^{\circ}\text{C}$; convection heat transfer coefficient $h=2,000$ $\text{W}/\text{m}^2\text{ }^{\circ}\text{C}$; phase change temperature: $1400\text{-}1410^{\circ}\text{C}$)

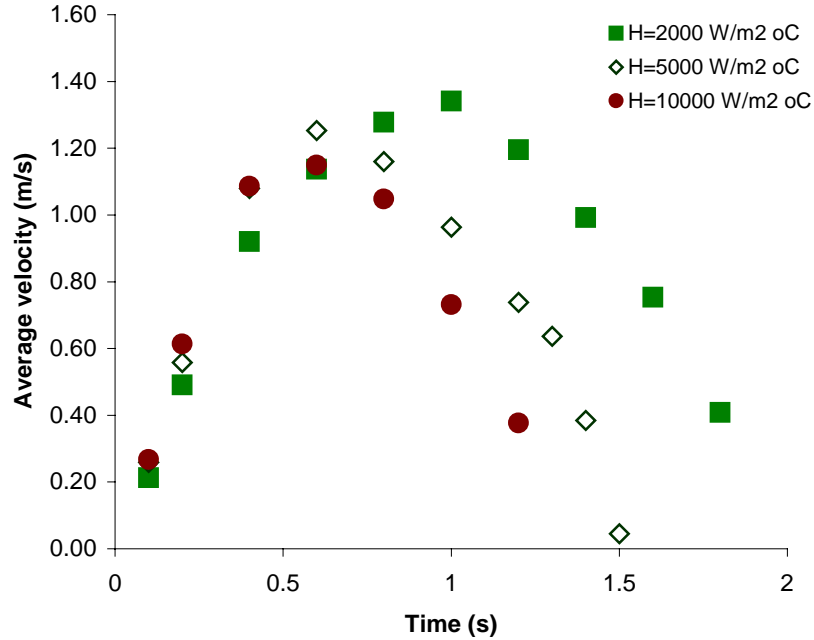


Figure 14 - Comparison of average filling velocity for different heat transfer coefficients (Inlet pressure: $P= 20,000$ Pa; inlet temperature= 1500°C ; mold preheated temperature: $T=400^{\circ}\text{C}$; phase change temperature: $1400\text{-}1410^{\circ}\text{C}$; mold material: copper)

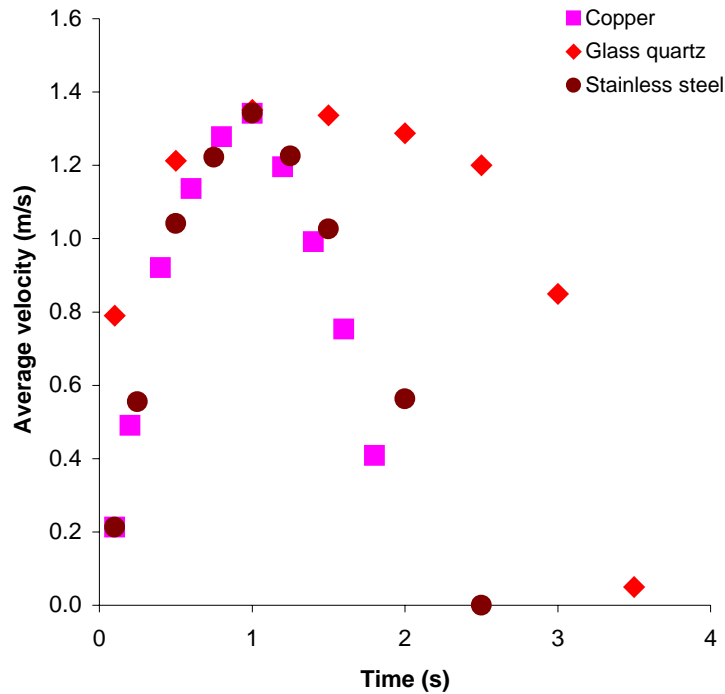


Figure 15 – Comparison of average velocity of the melt as it flows into the mold for different mold materials. (Inlet pressure: $P= 20,000$ Pa; inlet temperature= 1500°C ; mold preheated temperature: $T=400^{\circ}\text{C}$; phase change temperature: $1400\text{-}1410^{\circ}\text{C}$)

The second portion of this research work involves the detailed analysis of the filling of the mold by the melt. Figure 16 shows flow field results for the free surface filling of the mold. The Volume of Fluid (VOF) technique is used to simulate the flow entering the mold. Present research efforts include the coupled analysis of filling and solidification and will be completed shortly to finalize the model development for this task.

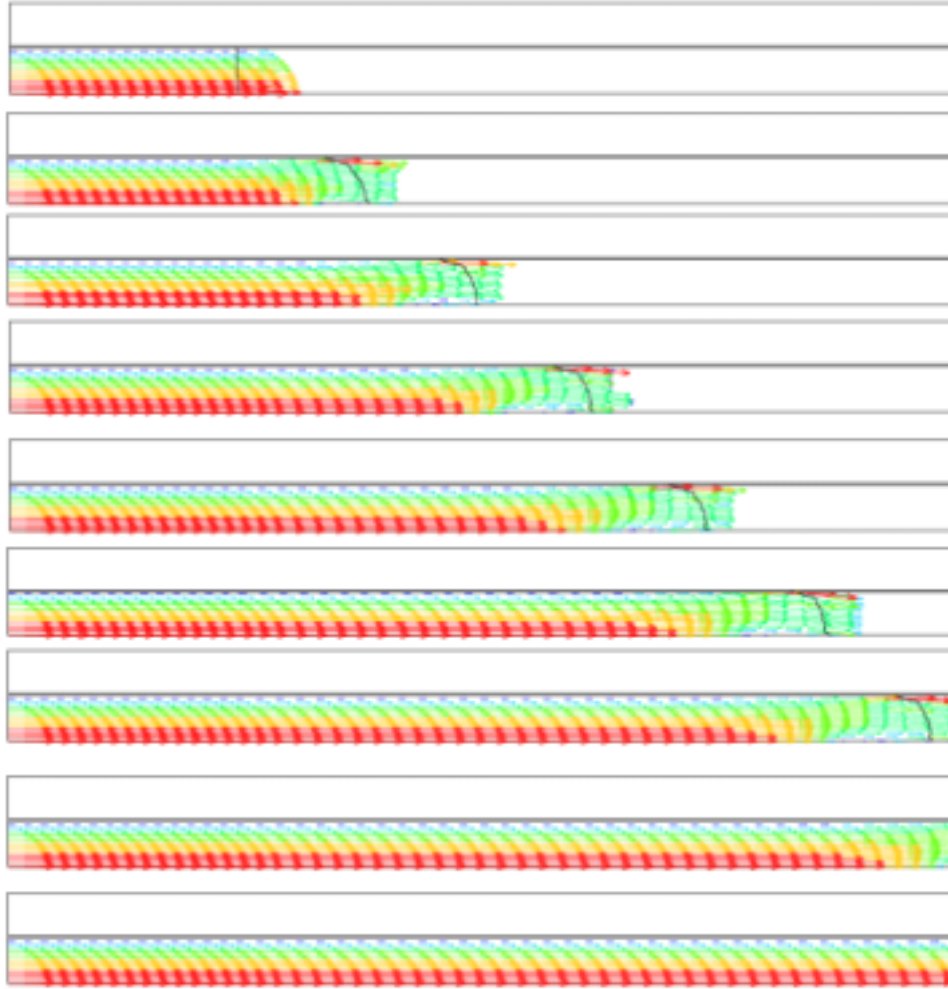


Figure 16 - Representative flow field for free surface flow into mold region (axisymmetric geometry shown). Solid line across the velocity vectors represents the fill front. (0.01 seconds between plots, Inlet velocity $V=0.5$ m/s, Mold material: copper, Inlet temperature: $1,500^{\circ}\text{C}$ Heat transfer coefficient $h=2,000$ $\text{W/m}^2\text{C}$ Mold preheated temperature 800°C)

3.2 Induction Heating Model

Modeling results for a representative design of a coil, crucible, cover and melt are presented. These results show the regions of high induction heating and demonstrate the ability of the model to properly analyze the system.

3.2.1. Modeling Results

Figure 17 shows the general layout for the system to be considered. The model includes the coils, crucible, melt, “cover,” and void space. The model will capture all of the relative physics that deal with mass transfer from the melt. The geometry shown is an axisymmetric model

where the centerline of this figure is on the right hand side of the drawing. The z-axis exists along the right side and runs from bottom to top.

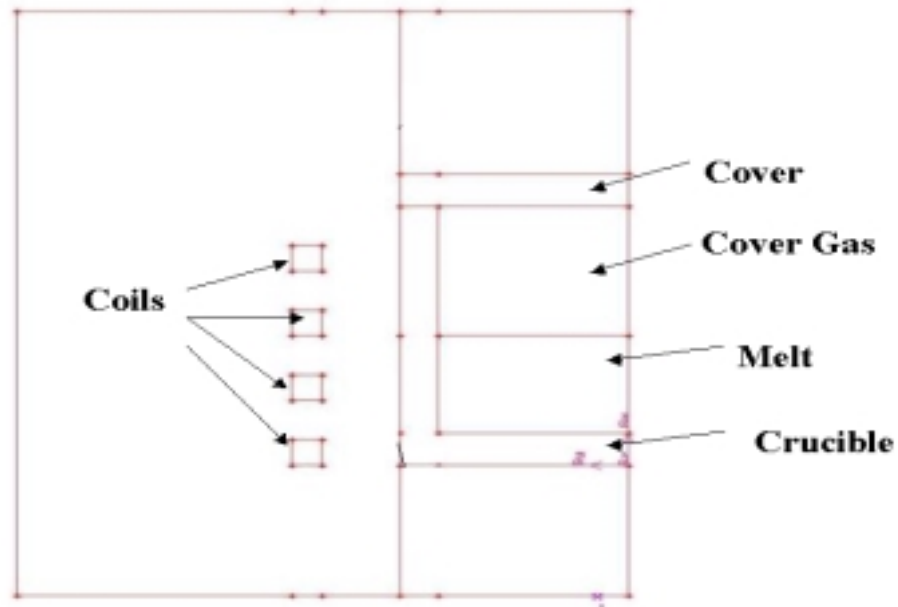


Figure 17 - Representative system model for ISM.

The axisymmetric model consisted of slightly over 10,000 elements. The mesh was compressed along the inner surface of the melt region near to the crucible. A small amount of coupling between the coils and the ISM will occur, but is limited because the coil segments are broken into sections, which disturbs the electrical field and prevents significant induction heating to occur in the crucible itself. The strongest amount of coupling will occur between the coils and the “melt” region, which is initially a solid that needs to be melted.

Figure 18 shows portions of the finite element mesh and highlights the geometric features of this model. These physical components are the coil, crucible, cover and the melt. Mesh was compressed near the outer edges (those near the coil) of the melt because this is the region where induction heating will occur – the thin layer near the outer surface.

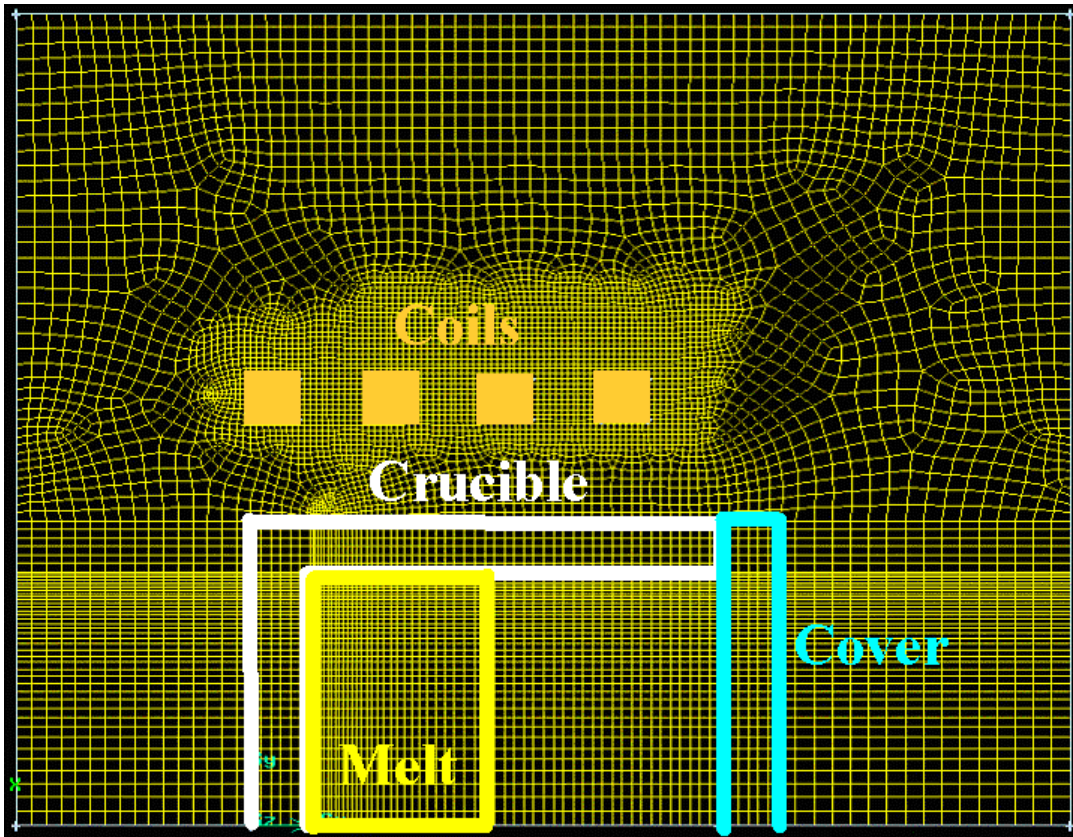


Figure 18 - Finite element mesh for the analysis of induction heating in an ISM system.

The field variables for the calculation of induction heating are C and S. The C variable is solved as “species 1” within FIDAP and the S variable is solved for as “species 2” in FIDAP. FIDAP has the ability to deal with 15 different species equations, hence the reason they are referred to as “1”, “2”, etc.

Previous analyses had assumed a continuous coil region. The current work considers a more realistic coil region where each segment of the coil is modeled. The number of coils, spacing, dimensions, etc. can all be considered in the analysis process.

Figures 19 and 20 present contours of the field variable C. The variable C has its peak values in the coil region. The contours of the center two coils are slightly higher than the two end coils. The surface plot of C clearly shows how it is only high within the coil region itself, dropping off rapidly in the other locations.

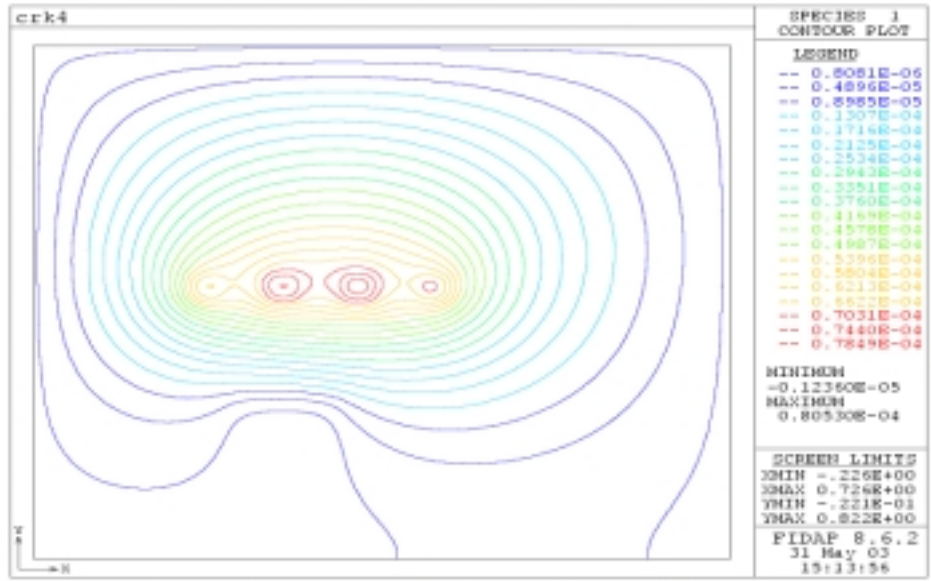


Figure 19 - Contour plots of the field variable C used in the calculation of the induction heating equation.

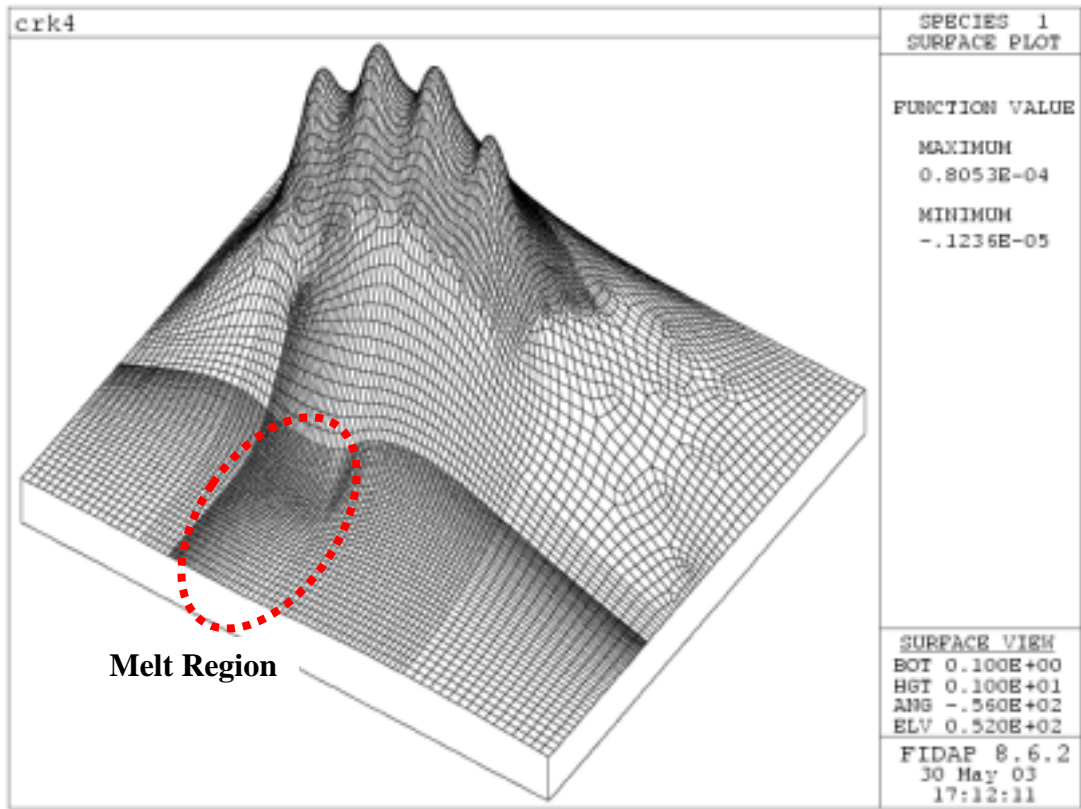


Figure 20 – Surface plot of the field variable C used in the calculation of the induction heating equation. Each peak resides at the location of a coil of the induction coil.

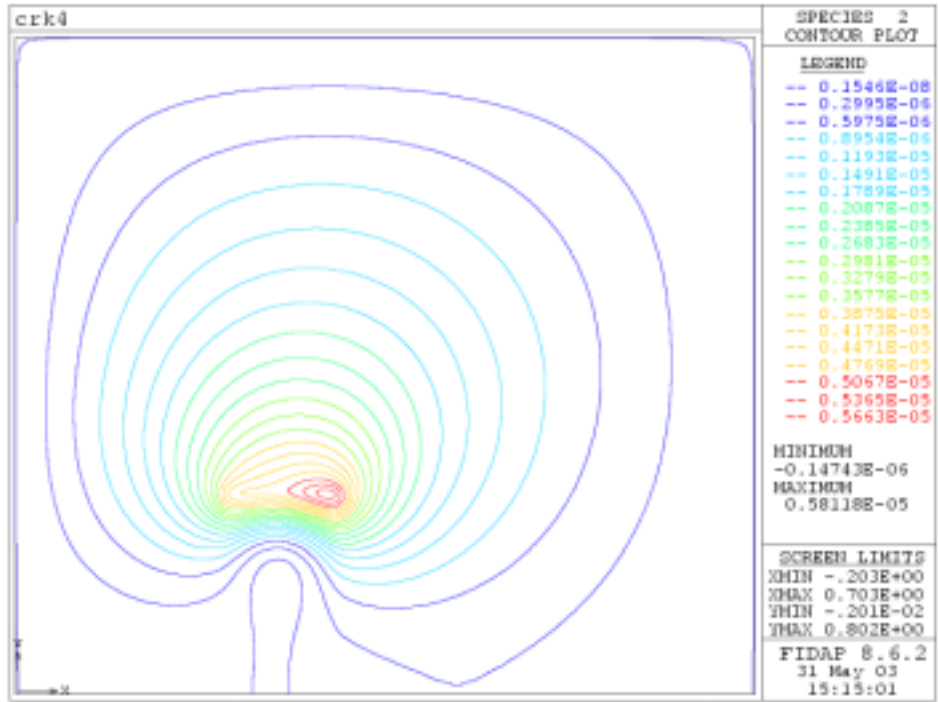


Figure 21 – Contours of field variable S (species 2) used in the calculation of the induction field. Peak occurs near the top edge of the melt region.

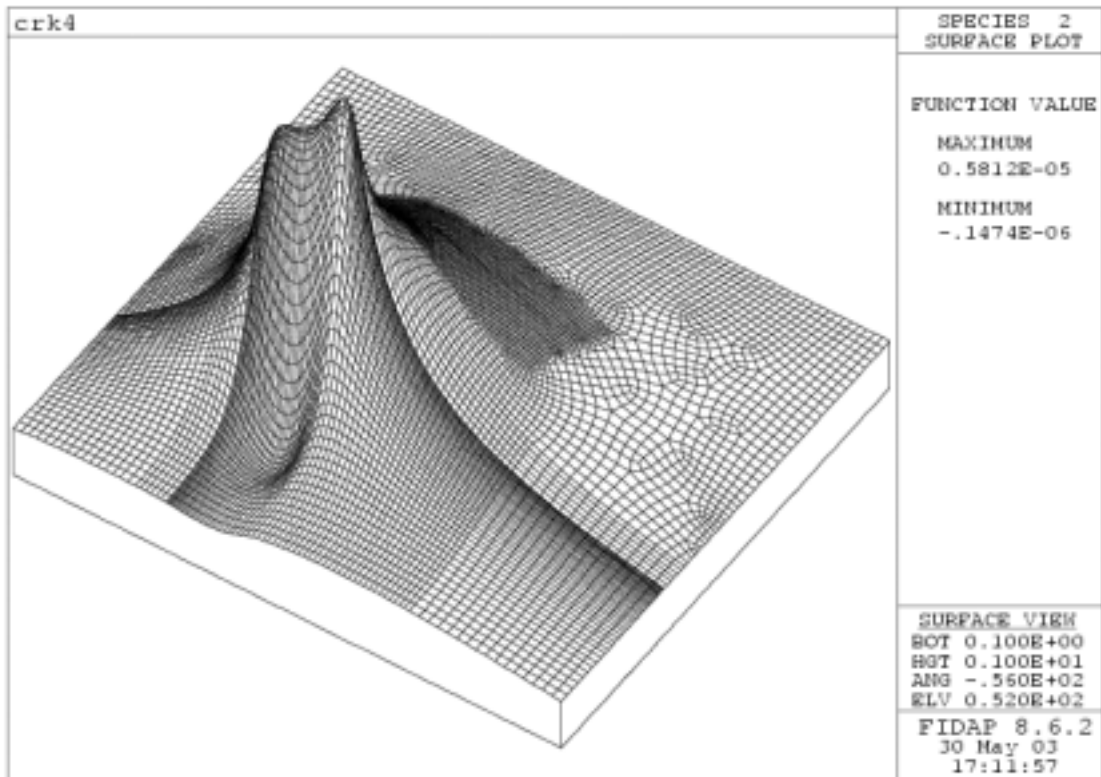


Figure 22 – Surface plot of induction heating field variable S. Peak occurs at the outer edge and top of the melt region.

Contour plots for the second field variable, S, are shown in Figures 21 and 22. Here, the peak value occurs near the top, outer edge of the melt region. This is the region where skin heating will occur as a result of the coupling of the fields.

The model has shown the ability to calculate the induction-heating field for typical geometries (coil, crucible, melt). Rapid heating is typically experienced in the region indicated by the high fluxes, resulting in the melting of the material within the ISM.

3.2.2. Theoretical Background

An important component in the development of an inductively heated casting furnace is the determination of the amount of heating produced by the system. Traditionally, detailed models of the electromagnetic field are used to evaluate the performance of the coil design. For the present problem, it is important to couple the produced field, heating, and fluid flow to insure proper mixing and to understand the mass transport from the melt into the gas space above the melt. The complete details of the model discussed here can be found in full in *Appendix B*.

Induction heating is commonly used in furnaces to melt metals for a number of metallurgical processes. This section of the report briefly discusses the governing. The resulting governing equations are shown below and are for a cylindrical geometry, but the equations are similar to a Cartesian coordinates form (see Appendix B for complete details).

In tensor notation the equations are reduced to those shown below.

$$\left. \begin{aligned} \nabla \cdot \left(\frac{1}{r} \nabla C \right) &= -\mu J_o \\ \nabla \cdot \left(\frac{1}{r} \nabla S \right) &= 0 \end{aligned} \right\} \text{Coil} \quad (15)$$

$$\left. \begin{aligned} \nabla \cdot \left(\frac{1}{r} \nabla C \right) &= \frac{\mu \sigma \omega}{r} S \\ \nabla \cdot \left(\frac{1}{r} \nabla S \right) &= -\frac{\mu \sigma \omega}{r} C \end{aligned} \right\} \text{Conductor} \quad (16)$$

$$\left. \begin{aligned} \nabla \cdot \left(\frac{1}{r} \nabla C \right) &= 0 \\ \nabla \cdot \left(\frac{1}{r} \nabla S \right) &= 0 \end{aligned} \right\} \text{Elsewhere} \quad (17)$$

where

- C, S = real and complex components of function substituted into governing equations to simplify solution process
- r = radial coordinate
- J_o = current density
- μ = permeability
- ω = frequency
- σ = electrical conductivity

Using the appropriate relationships and integrating gives the heat deposition as a function of position.

$$Q(r, z) = \frac{\sigma\omega^2}{2r^2} [S^2 + C^2] \quad (18)$$

3.3 Mass Transfer Model

The mass transfer of the americium from the melt is an important consideration in the complete project. The mass transfer is best described by the schematic shown in Figure 23. References 20 through 45 were used for the development of the mass transfer model as it is presented here. The model requires the consideration and interaction of three phenomena.

- Mass transport within the melt to the interface region (item 1 in Figure 23). This effectively reduces to transport through a thin boundary layer type region at the surface of the melt. The mass transport coefficient is defined as β_m (cm/sec).
- Vaporization across the interface (item 2 in Figure 23). The mass transfer coefficient for this step is defined as K_m (cm/sec).
- Mass transport within the gas phase above the melt (item 3 in Figure 23). The mass transport coefficient for this step is defined as β_g (cm/sec).

The liquid boundary layer is step 1 is assumed to follow Machlin's model and can be defined as

$$\beta_m = 2\sqrt{2Dv/\pi r} \quad (19)$$

where

- D = diffusion coefficient
- v = speed of melt in boundary layer.
- r = Machlin mode.

Each of these values can be estimated for the present system of interest.

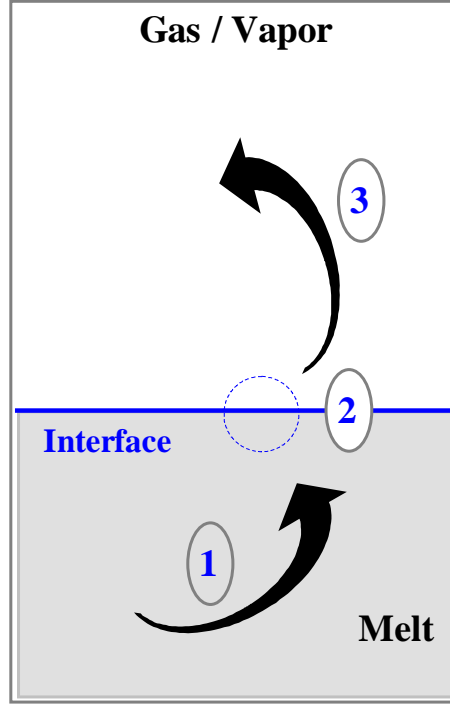


Figure 23 - Mass transport consists of (1) transport within the melt, (2) vaporization at the interface, and (3) transport in the gas phase.

The mass transfer rate across the interface (2) can be written as

$$N_m = K_m C_{ms(i)} = K_L \varepsilon (P_{e(i)} - P_{g(i)}) \sqrt{M_i / T_{ms}} \quad (20)$$

Accordingly, this allows the mass transfer coefficient to be written as

$$K_m = \frac{K_L \varepsilon (P_{e(i)} - P_{g(i)}) \sqrt{M_i / T_{ms}}}{C_{ms(i)}} \quad (21)$$

where

- T_{ms} = temperature of the evaporating surface.
- $P_{e(i)}$ = equilibrium partial pressure of component i at temperature T_{ms}
- $P_{g(i)}$ = partial pressure of component i in the gas space.
- K_L = Langmuir constant.
- $C_{ms(i)}$ = average content of component i on the surface of the melt.
- M_i = atomic weight of component i .
- ε = condensation coefficient (1 for metals).

The components equilibrium partial pressure is defined as $P_{e(i)} = x_i \gamma_i P_i^o$, where P_i^o is the equilibrium pressure of pure substance i and x_i is the mole fraction of component i . The challenge for americium in our system is to evaluate γ_i , the activity coefficient.

Appendix A contains the complete details for the model development. The activity coefficient can ultimately be determined from the relationship shown below.

$$\begin{aligned}
\ln \gamma_i = & \frac{\alpha_{ij} f_{ij}}{RT} \left[\left(\frac{x_i [1 + u_i x_j (\phi_i - \phi_j)] x_j [1 + u_j x_i (\phi_j - \phi_i)]}{x_i [1 + u_i x_j (\phi_i - \phi_j)] V_i^{\frac{2}{3}} + x_j [1 + u_j x_i (\phi_j - \phi_i)] V_j^{\frac{2}{3}}} \right) + \right. \\
& (1 - x_i) \left\{ \frac{(1 + u_i x_j (\phi_i - \phi_j))(1 + x_i u_j (\phi_j - \phi_i))}{(1 + u_i x_j (\phi_i - \phi_j)) x_j V_i^{\frac{2}{3}} + (1 + u_j x_i (\phi_j - \phi_i)) x_i V_j^{\frac{2}{3}}} + \right. \\
& \left. \left(\frac{x_i (1 + u_i x_j (\phi_i - \phi_j)) x_j u_j (\phi_j - \phi_i)}{x_i (1 + u_i x_j (\phi_i - \phi_j)) x_j V_i^{\frac{2}{3}} + (1 + u_j x_i (\phi_j - \phi_i)) x_j V_j^{\frac{2}{3}}} \right) - \right. \\
& \left. \left(\frac{x_i (1 + u_i x_j (\phi_i - \phi_j)) x_j (1 + x_i u_j (\phi_j - \phi_i))}{\left(x_i (1 + u_i x_j (\phi_i - \phi_j)) x_j V_i^{\frac{2}{3}} + (1 + u_j x_i (\phi_j - \phi_i)) x_j V_j^{\frac{2}{3}} \right)^2} \right) \times \right. \\
& \left. \left. \left((1 + u_i x_j (\phi_i - \phi_j)) x_j V_i^{\frac{2}{3}} + u_j (\phi_j - \phi_i) x_j V_j^{\frac{2}{3}} \right) \right\} \right] \quad (22)
\end{aligned}$$

The variables used in Equation 22 are defined and discussed in detail in Appendix A. The complete equation is only shown here to demonstrate the complexity of the solution.

The activities of Am in molten U-Am and Pu-Am will be calculated. The controlling steps of mass transfer process will also be studied in year three. Previous research efforts were focused on the transport to the melt surface and the evaporation at that interface. The additional two stages of transport are also important in the present work. The transport of the vapor through the gas phase and eventual deposition on surrounding surfaces is important. Knowing where the americium will deposit or where it will be transported is a major concern.

4. Summary

The phase II work shows the process and progress of establishing the important steps of casting metallic fuel pin furnace modeling. Three major modeling of casting rod heat transfer, induction heating model, and mass transfer model have been studied. The filling and solidification process for melt casting a metallic fuel pin have also been extensively scrutinized. The model was analyzed numerically using the commercial finite element software package FIDAP (Fluent, Inc.). Numerical simulations were performed to study process parameters that could impact the

solidification of the melt within the mold. A Metallic Fuel Pin mold is a long, thin, straw-like pipe, which has a cylindrical shape. The fluid is a high-temperature melt mixture of Am, Pu, and Zr, which is considered as an incompressible Newtonian fluid. Filling velocities and filling pressures are varied to study what impact these parameters might have on flow and solidification within the melt. The induction heating model results for a representative design of a coil, crucible, cover and melt were also studied. These results show the regions of high induction heating and demonstrate the ability of the model to properly analyze the system. The induction heating model has shown the ability to calculate the induction-heating field for typical geometries (coil, crucible, melt). Rapid heating is typically experienced in the region indicated by the high fluxes, resulting in the melting of the material within the ISM. The mass transport model has also been set up and studied. It consists of transport within the melt, i.e., mass transport within the melt to the interface region, vaporization at and across the interface, i.e., and mass transport in the gas phase.

5. References

1. Dynamic Analysis of An overhead Crane Carrying A Canister By Finite Element Method –Musukula, University of Nevada, Las Vegas, 1993.
2. <http://apt.lanl.gov/atw/index.html>, (March 21, 2002).
3. <http://www.nuc.berkeley.edu/designs/ifr>, (April 4, 2002).
4. Compilation of Information on Modeling of Inductively Heated Cold Crucible Melters, D.L. Lessor, March 1996.
5. Injection casting of U-Zr-Mn, surrogate alloy for U-Pu-Zr-Am-Np, C.L., Journal of Nuclear Materials 224(1995) 305-306.
6. The Induct slag Melting Process, P.G. Clites, (Bulletin/United States Department of the Interior, Bureau of Mines, 673), 1982.
7. Induction Skull Melting of Titanium Aluminides, P.G. Breig and S.W. Scott, the Duriron Company, Inc. 1989
8. Hazardous waste & Hazardous materials, Volume 11, Number 1, 1994 (what is the title of the article? The author?)
9. The ABB DC arc furnace: Past, present, future, S.E. Stenkvis (ABB Process Automation), June 1992
10. A Simplified Thermal Analysis of an Inductively Heated Casting Furnace, Randy Clarksean and Charles Solbrig, ASME Heat Transfer Division, Vol. 317-1, pp. 433-441

11. Crucible for Induction Melting, Wilfried Guy, Kelsterbach, Germany, July, 1995 Journal?
12. Crucible for The Inductively Melting of Metals, Matthias Blum, Bodingen Wilfried Goy, Kelsterbach, Frauz Hage, Germany, Oct., 1996
13. Cold Crucible Type Levitation Melting of Reactive Metals, A. Fukuzawa Chemical Processing Division (this is not a complete reference)
14. The Further Development of the Semilevitation Melting Technique for The Production of Casting in Reactive Alloys, R A Harding and X R Zhu, University of Birmingham, UK.
15. Cook, R. D., Malkus, D.S. and Plesha, M.E., "Concepts and applications of finite element analysis", John Wiley & Sons, New York, 1989, Third edition.
16. Hirt, C.W. and Nichols, B.D., "Volume of Fluid (VOF) Method for the Dynamics of Free Boundaries," *Journal of Computational Physics* 39, 201, 1981.
17. S.Kvicinsky, F. Longatte, J.-L. Kueny and F. Avellan, "Free Surface Flows: Experimental Validation of Volume of Fluid (VOF) Method in the Plane Wall Case", *Proceedings of the 3rd ASME/JSME Joint Fluids Engineering Conference*, July 18-23 1999, San Francisco, California
18. Nichols, B.D. and Hirt, C.W., "Methods for Calculating Multi-Dimensional, Transient Free Surface Flows Past Bodies," *Proc. First Intern. Conf. Num. Ship Hydrodynamics*, Gaithersburg, ML, Oct. 20-23, 1975
19. C.A. Santos, J.M.V. Quaresma, A. Garcia, "Determination of transient interfacial heat transfer coefficient in chill mold castings", *Journal of Alloys and Compounds* 319 (2001), 174-186.
20. Harris, R., and Davenport, W.G., 1982, "Vacuum Distillation of Liquid Metals: Part 1. Theory and Experimental Study," *Metallurgical Transactions B*, vol. 13B, December, pp. 581-88.
21. Harris, R., and Davenport, W.G., 1982, "Vacuum Distillation of Liquid Metals: Part 1. Photographic Study," *Metallurgical Transactions B*, vol. 13B, December, pp. 589-91.
22. Ozberk, E., and Guthrie, R.I.L., 1985, "Evaluation of Vacuum Induction Melting of Copper Refining," *Transactions of the Institution of Mining and Metallurgy Section C Mineral Processing and Extractive Metallurgy*, vol 94, September, pp. C146-C157.
23. Ozberk, E., and Guthrie, R.I.L., 1986, "A Kinetic Model for the Vacuum Refining of Inductively Stirred Copper Melts," *Metallurgical Transactions B*, vol. 17B, March, pp. 87-103.

24. Hino, M., Wand, S., Nagasaka, T., and Ban-ya, S., 1994, "Evaporation Rate of Zinc in Liquid Iron," *ISIJ International*, vol. 34, no. 6, pp. 491-97.
25. Li, L., Tu, S., and Janke, D., 1995, "Kinetics of Zn and Pb Evaporation from Liquid Iron," *Steel Research*, vol. 66, no. 5, pp. 188-93.
26. Guo, J., Yuan, L. Yanqing, S., Hongsheng, D., and Jun, J., 1998, "Evaporation Behavior of Components in Ti-15-3 Melt During ISM Process," *Transactions of Nonferrous Metals Society of China*, vol. 8, no. 4, pp. 539-43.
27. Guo, J., Liu, Y., Su, Y., Ding, H., Liu, G., and Jia, J., 1999, "Evaporation Behavior of Aluminum During the Cold Crucible Induction Skull Melting of Titanium Aluminum Alloys," *Metallurgical and Materials Transactions B*, vol 31B, August, pp. 837-44.
28. Savov, L. and Janke, D., 2000, "Evaporation of Cu and Sn from Induction-Stirred Iron-Based Melts Treated at Reduced Pressure," *ISIJ International*, vol. 40, no. 2, pp. 95-104.
29. Guo, J., Liu, G., Su, Y., Liu, Y., Ding, H.S., and Jia, J., 2000, "Control of Al Content during ISM Process of Nb_3Al ," *Transactions of Nonferrous Metals Society of China*, vol. 10, no. 5, pp. 571-75.
30. Bellot, J.P., Duval, H., Ritchie, M., Mitchell, A., and Ablitzer, D., 2001, "Evaporation of Fe and Cr from Induction-Stirred Austenitic Stainless Steel. Influence of Inert Gas Pressure," *ISIJ International*, vol. 41, no. 7, pp. 696-705.
31. Gokcen, N.A., 1986, *Statistical Thermodynamics of Alloys*, Plenum Press, New York.
32. Saito, T. (editor), 1999, *Computational Materials Design*, Springer, London.
33. Ilegbusi, O.J., Iguchi, M., and Wahnsiedler, W., 2000, *Mathematical and Physical Modeling of Materials Processing Operations*, Chapman and Hall (CRC), Boca Raton, Florida.
34. Liw, H. and Bouchard, M., 1997, "Evaluation of Interaction Coefficient in Al-Cu-H Alloy," *Metallurgical and Materials Transactions B*, vol. 28B, August, pp. 625-632.
35. Waseda, Y., Ueno, S., and Toguri, J.M., 1989, "Theoretical Calculation of Solute Activity Coefficient at Infinite Dilution in Metallic Solution," *Zeitschrift fur Metallkunde*, vol. 80, no. 6, pp. 406-12.
36. Ogawa, T., 1993, "Alloying Behavior Among U, Np, Pu, and Am Predicted with the Brewer Valence Bond Model," *Journal of Alloys and Compounds*, vol. 194, pp. 1-7.
37. Dubinin, N.E., Yuryev, A.A., and Vatolin, N.A., 1995, "Thermodynamic Properties of Ternary Liquid Metal Alloys," *High Temperature Materials and Processes*, vol. 14, no. 4, pp. 285-290.

38. Wang, F.M., Li, X.P., Han, Q.Y., and Zhang, N.X., 1997, "A Model for Calculating Interaction Coefficients Between Elements in Liquid and Iron-Base Alloy," *Metallurgical and Materials Transactions B*, vol. 28B, February, pp. 109-113.
39. Ueno, S., Waseda, Y., Jacob, K.T., and Tamaki, S., 1988, "Theoretical Treatment of Interaction Parameters in Multicomponent Metallic Solutions," *Steel Research*, vol 59, no. 11, pp. 474-83.
40. Toop, G.W., 1965, "Predicting Ternary Activities Using Binary Data," *Transactions of the Metallurgical Society of AIME*, vol. 233, pp. 850-55.
41. Sherwood, T.K., and Cooke, N.E., 1957, "Mass Transfer at Low Pressures," *A.I.Ch.E. Journal*, vol. 3, no. 1, pp. 37-42.
42. Tanaka, T., Gokcen, N.A., and Morita, Z., 1990, "Relationship Between Enthalpy of Mixing and Excess Entropy in Liquid Binary Alloys," *Zeitschrift fur Metallkunde*, vol. 81, no. 1, pp. 49-54.
43. Tanaka, T., Gokcen, N.A., Spencer, P.J., Morita, Z., and Iida, T., 1993, "Evaluation of Interaction Parameters in Dilute Liquid Ternary Alloys by a Solution Method Based on the Free Volume Theory," *Zeitschrift fur Metallkunde*, vol. 84, no. 2, pp. 100-05.
44. Pehlke, R.D., 1973, *Unit Processes of Extractive Metallurgy*, American Elsevier Publishing Company, Inc., New York.
45. Turkdogan, E.T., 1980, *Physical Chemistry of High Temperature Technology*, Academic Press, New York.
46. Akinlade, O., and Sommer, F., 2001, "Concentration Fluctuations and Thermodynamic Properties of Ternary Liquid Alloys," *Journal of Alloys and Compounds*, vol. 316, pp. 226-235.
47. Su, Y., Guo, J., Ding, H., Liu, S., Liu, Y., Liu, G., and Jia, J., 2001, "Component Evaporation of Ti-15-3 Melt During ISM Processing," *Journal of Materials Science and Technology*, vol. 17, no. 1, pp. 83-4.
48. Gokcen, N.A., 1997, "Thermodynamics of Solutions: A Unified Concept," *J Chim Phys*, vol. 94, pp. 817-843.
49. Maeda, M., Kiwake, T., Shibuya, K., and Ikeda, T., 1997, "Activity of Aluminum in Molten Ti-Al Alloy," *Materials Science and Engineering*, vol. A239-240, pp. 276-80.
50. Ma, Z., 2000, "Thermodynamic Description for Concentrated Metallic Solutions Using Interaction Parameters," *Metallurgical and Materials Transactions B*, vol 32B, February, pp. 87-103

51. Ding, X., Fan, P., and Wang, W., 1999, "Thermodynamic Calculation for Alloy Systems," *Metallurgical and Materials Transactions B*, vol. 30B, April, pp. 271-77.
52. Gokcen, N.A., Tanaka, T., and Morita, Z., 1993, "Atomic Theories on Energetics of Alloy Formation," *J Chim Phys*, vol. 90, pp. 233-248.
53. Turkdogan, E.T., Grieveson, P., and Darken, L.S., 1963, "Enhancement of Diffusion-Limited Rates of Vaporization of Metals," *J. Phys. Chem.*, vol. 67, August, pp. 1647-54.
54. Miedema, A.R., de Chatel, P.F., de Boer, F.R., 1980, "Cohesion in Alloys - Fundamentals of a Semi-Empirical Model," *Physica*, vol. 100B, pp. 1-28.
55. Ferro, R., Cacciamani, G., Saccone, A., and Borzone, G., "Systematics of Lanthanide and Actinide Compound Formation: Remarks on the Americium Alloying Behaviour," *Journal of Alloys and Compounds*, vol. 320, pp. 326-40.
56. Ogawa, T., Ohmichi, T., Maeda, A., Arai, Y., and Suzuki, Y., 1995, "Vaporization Behaviour of (Pu, Am)N," *Journal of Alloys and Compounds*, vol 224, pp. 55-59.

6. Appendices